

PAPER • OPEN ACCESS

3D MHD modelling of plasmoid drift following massive material injection in a tokamak

To cite this article: M. Kong et al 2025 Nucl. Fusion 65 016042

View the <u>article online</u> for updates and enhancements.

You may also like

- The role of ion-scale micro-turbulence in pedestal width of the DIII-D wide-pedestal
- Zeyu Li, Xi Chen, Xiang Jian et al.
- Impurity transport driven by kinetic ballooning mode in the strong gradient pedestal of tokamak plasmas Shanni Huang, Weixin Guo and Lu Wang
- Non-linear dependence of ion heat flux on plasma density at the L-H transition of JET NBI-heated deuterium-tritium plasmas
 P. Vincenzi, E.R. Solano, E. Delabie et al.



Nucl. Fusion 65 (2025) 016042 (14pp)

https://doi.org/10.1088/1741-4326/ad96ca

3D MHD modelling of plasmoid drift following massive material injection in a tokamak

M. Kong^{1,*}, E. Nardon², D. Bonfiglio³, M. Hoelzl⁴, D. Hu⁵, the JOREK Team^a, JET Contributors^b and the EUROfusion Tokamak Exploitation Team^c

- ¹ École Polytechnique Fédérale de Lausanne (EPFL), Swiss Plasma Center (SPC), CH-1015 Lausanne, Switzerland
- ² CEA, IRFM, F-13108 Saint-Paul-lez-Durance, France
- ³ Consorzio RFX and CNR-ISTP, Corso Stati Uniti 4, 35127 Padova, Italy
- ⁴ Max Planck Institute for Plasma Physics, Boltzmannstr. 2, 85748 Garching b. M., Germany
- ⁵ School of Physics, Beihang University, Beijing 100191, China

E-mail: mengdi.kong@epfl.ch

Received 30 July 2024, revised 13 October 2024 Accepted for publication 25 November 2024 Published 6 December 2024



Abstract

Mechanisms of plasmoid drift following massive material injection are studied via 3D non-linear MHD modelling with the JOREK code, using a transient neutral source deposited at the low field side midplane of a JET H-mode plasma to clarify basic processes and compare with existing theories. The simulations confirm the important role of the propagation of shear Alfvén wave (SAW) packets from both ends of the plasmoid ('SAW braking') and the development of external resistive currents along magnetic field lines ('Pégourié braking') in limiting charge separation and thus the $\mathbf{E} \times \mathbf{B}$ plasmoid drift, where \mathbf{E} and \mathbf{B} are the electric and magnetic fields, respectively. The drift velocity is found to be limited by the SAW braking on the few microseconds timescale for cases with relatively small source amplitude while the Pégourié braking acting on a longer timescale is shown to set in earlier with larger toroidal extent of the source, both in good agreement with existing theories. The simulations also identify the key role of the size of the $\mathbf{E} \times \mathbf{B}$ flow region on plasmoid drift and show that the saturated velocity caused by dominant SAW braking agrees well with theory when considering an effective pressure within the $\mathbf{E} \times \mathbf{B}$ flow region. The existence of SAWs in the simulations is demonstrated and the 3D picture of plasmoid drift is discussed.

- ^a See Hoelzl et al 2024 (https://doi.org/10.1088/1741-4326/ad5a21) for the JOREK Team.
- b See Maggi et al 2024 (https://doi.org/10.1088/1741-4326/ad3e16) for JET Contributors.
- ^c See Joffrin *et al* 2024 (https://doi.org/10.1088/1741-4326/ad2be4) for the EUROfusion Tokamak Exploitation Team.
- Author to whom any correspondence should be addressed.



Original Content from this work may be used under the terms of the Creative Commons Attribution 4.0 licence. Any

further distribution of this work must maintain attribution to the author(s) and the title of the work, journal citation and DOI.

Keywords: massive material injection, plasmoid drift, disruption, MHD modelling, JOREK

(Some figures may appear in colour only in the online journal)

1. Introduction

The ablation of a cryogenic pellet or pellet fragment in the case of shattered pellet injection (SPI) in tokamak plasmas generates a high density and pressure plasmoid, where SPI is one type of massive material injection (MMI) methods and the current concept for the ITER disruption mitigation system (DMS) to mitigate the detrimental effects of plasma disruptions [1]. It is well known from hydrogen isotope pellet fuelling experiments that the ablation plasmoid moves towards the tokamak low field side (LFS) due to the $\mathbf{E} \times \mathbf{B}$ drift originating from a vertical polarization induced inside the plasmoid by the ∇B drift [2-9, and references therein], where E and B are the electric and magnetic fields, respectively. This has also been highlighted in recent 3D MHD modelling of deuterium (D₂) SPI experiments on JET, demonstrating that plasmoid drift could affect the effectiveness of disruption mitigation with LFS D₂ SPI [10].

As illustrated in figure 1(a), the charge separation resulting from the ∇B drift (represented by $\mathbf{j}_{\nabla B}$ shown in red) can only be compensated, on a very short timescale, by a polarization current (\mathbf{j}_{pol} in green) associated to the acceleration of the plasmoid towards the LFS [4]. Here $\mathbf{j}_{\nabla B} = 2(p_0 - p_\infty)\mathbf{B} \times \nabla B/B^3$ and $\mathbf{j}_{pol} = (n_0 m_i/B^2)\mathrm{dE}/\mathrm{dt}$, where p_0 and p_∞ refer to the total (electron and ion) plasmoid and background plasma pressure, respectively, $n_0 = n_e$ is the plasmoid electron density, m_i the ion mass and B the magnetic field strength. Note that in figure 1 we have only showed two magnetic field lines (marked as ① and ②) connecting the top and bottom of the plasmoid (purple contour) for simplicity.

On longer timescales, two 'braking' mechanisms have been identified in theory and are expected to play an important role in limiting plasmoid drift. One is the propagation of shear Alfvén wave (SAW) packets from both ends of the plasmoid at the Alfvén speed $C_A \equiv B/\sqrt{\mu_0 n_\infty m_i}$ [4, 5], where μ_0 is the magnetic permeability and n_{∞} the background electron density. This allows the charges to flow externally to the plasmoid and is denoted as 'SAW braking' hereafter. The current related to the SAW propagation is $j_A = -\nabla^2_{\perp} A_{\parallel}/\mu_0 =$ $-\nabla^2 \Phi/(\mu_0 C_A)$ [4], where A_{\parallel} is the wave magnetic vector potential and Φ refers to the electrostatic potential that is proportional to the $\mathbf{E} \times \mathbf{B}$ flow potential (U). As illustrated in figure 1(b), the currents flow first in the parallel direction (with respect to the magnetic field), then in the perpendicular direction via \mathbf{j}_{pol} at the acceleration location associated to the charge propagation by the SAW packets, and then in the parallel direction again, flowing back into the plasmoid.

Based on the requirement that the divergence of the plasma current is zero, the early acceleration of plasmoid drift considering only the SAW braking has been derived by theory using cylindrical coordinates [4, 5]. In particular, an equation of

the magnetic-field-line-integrated electrostatic potential was obtained, which eventually allowed evaluating the acceleration and velocity of plasmoid drift. For instance, the acceleration of a single plasmoid along the drift direction (\dot{V}_D) is given by equation (1) [6]:

$$\dot{V}_D = \frac{2(p_0 - p_\infty)}{n_0 m_i R} - V_D \frac{2B_\phi^2}{\mu_0 C_A n_0 m_i Z_0},\tag{1}$$

where the first term on the right hand side (RHS) results from the balance between the ∇B current and the polarization current and the second term represents the SAW braking. R is the major radius, B_{ϕ} the toroidal magnetic field strength and Z_0 the half-length of the plasmoid along the magnetic field line. Considering $p_0 \gg p_{\infty}$ at the early phase of plasmoid expansion, one could obtain the saturated drift velocity $(V_{\rm D,lim})$ under the effect of the SAW braking based on equation (1), i.e.

$$V_{\rm D,lim} \approx \frac{\mu_0 C_A p_0 Z_0}{R B_\phi^2}.$$
 (2)

In particular, figure 1(b) corresponds to the situation where the SAW braking balances the charge separation, i.e. the RHS terms of equation (1) cancel out and the drift velocity V_D reaches $V_{D,\lim}$.

The other braking mechanism on the longer timescale is the development of external and purely parallel resistive currents (\mathbf{j}_{\parallel}) that connect the top and bottom of the plasmoid after the SAWs propagating in two different directions have run back to the plasmoid and is referred to as 'Pégourié braking' hereafter [6]. This suppresses the charge separation and plasmoid drift completely, as illustrated in figure 1(c). It follows that the Pégourié braking occurs on a longer time scale than the SAW braking and is strongly related to the toroidal extent of the plasmoid as it affects the external plasmoid-plasmoid connection length (L_{con}).

3D MHD codes, as has been demonstrated previously [11–14], contain relevant physics for modelling plasmoid drift. However, limitations on their achievable toroidal resolution make it challenging to quantitatively resolve experimentally relevant ablation plasmoids, for example, those generated by SPI. To investigate this size effect and clarify the underlying physics of plasmoid drift following MMI in tokamaks, we present 3D MHD simulations with the JOREK code [15, 16], using a transient neutral source deposited at the LFS midplane of a JET H-mode plasma. In particular, we aim at a detailed qualitative and quantitative comparison of 3D MHD simulations with existing plasmoid drift theories, which is done for the first time.

The rest of the paper is structured as follows. Section 2 describes the numerical model and setup used in the JOREK

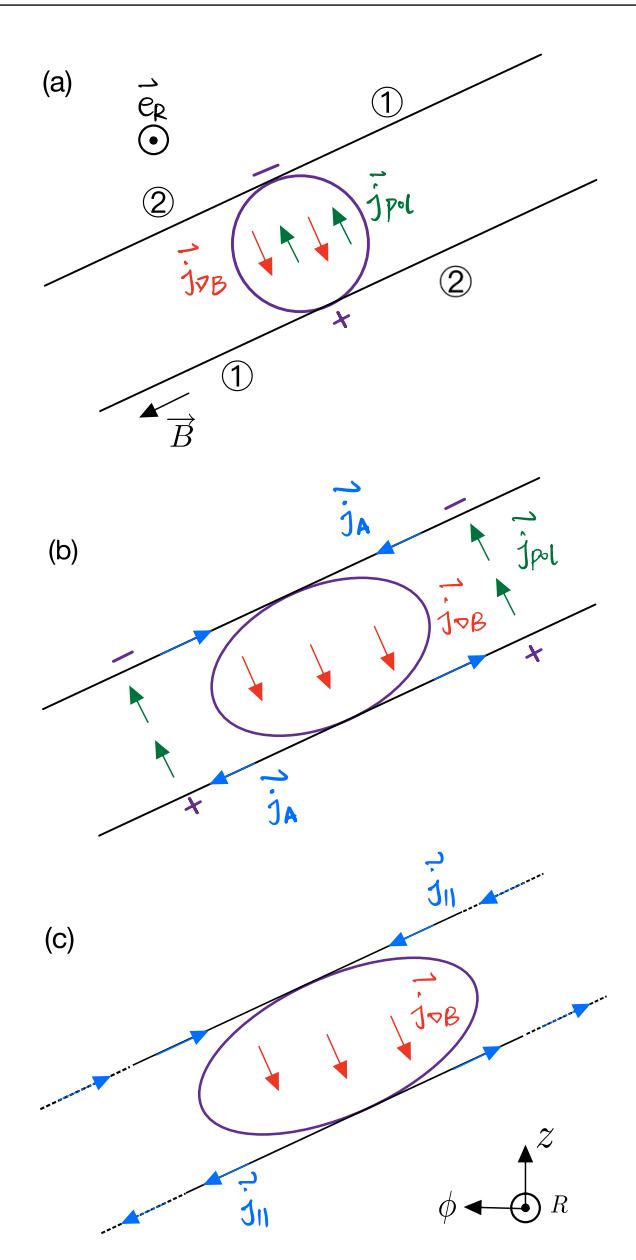


Figure 1. Sketch of plasmoid drift mechanisms of an initially spherical plasmoid and seen from the tokamak LFS along the R direction. (a) At t=0, (b) at $t < L_{\rm con}/(2C_A)$ and when $\dot{V}_D=0$ is reached via the SAW braking and (c) at $t \gg L_{\rm con}/(2C_A)$ when 3D parallel resistive currents suppress the charge separation and plasmoid drift, where $L_{\rm con}$ is the external plasmoid–plasmoid connection length. The symbols are elaborated in the text.

simulations. Section 3 presents JOREK modelling results and comparison with theory, where the effects of the source amplitude, source toroidal size and $\mathbf{E} \times \mathbf{B}$ flow region are investigated in detail and the 3D picture of plasmoid drift based on existing theories and JOREK simulations is also discussed. Section 4 demonstrates the existence of SAWs in the simulations, both qualitatively and quantitatively. Section 5 summarizes the main results of the paper and proposes possible future work.

2. Numerical model and simulation setup

The JOREK model used comprises ansatz-based reduced MHD equations with parallel flows and a fluid extension for neutrals. The poloidal magnetic flux, toroidal current density, poloidal flow potential, toroidal vorticity, plasma mass density, total plasma (ion and electron) pressure, parallel velocity and neutral mass density are evolved, while $\nabla \cdot \mathbf{B} = 0$ and $\nabla \cdot \mathbf{j} = 0$ are exactly satisfied, as detailed in [15–18]. JOREK also offers full MHD models [19] and kinetic full-f PiC models for neutrals [20], though not used in this paper.

The initial equilibrium remains the same as [10], i.e. taken from a JET H-mode plasma (#96874) with $R=2.96\,\mathrm{m}$, plasma current $I_p\approx 3\,\mathrm{MA}$, on-axis toroidal magnetic field $B_{\phi0}\approx 2.8\,\mathrm{T}$, thermal energy $W_{\mathrm{th}}\approx 7\,\mathrm{MJ}$, central electron temperature $T_{\mathrm{e}0}\approx 7\,\mathrm{keV}$ and central electron density $n_{\mathrm{e}0}\approx 0.85\times 10^{20}\,\mathrm{m}^{-3}$. The initial flux-surface-averaged n_e , T_e and q profiles used in JOREK simulations are shown in figure 2, where q is the safety factor and the horizontal axis ψ_N refers to the normalized poloidal magnetic flux. The ion temperature (T_i) is set to be the same as T_e in these simulations. The computational grid on the poloidal plane is the same as [10] (figure 7 there). Toroidal harmonics up to n=10 are included, which is sufficient to resolve the low n modes (n<3) that are dominant in these simulations. We use a fixed-boundary equilibrium, while an ideal wall is imposed for all harmonics.

Spitzer resistivity $\eta_{\rm sp} \left[{\bf \Omega \cdot m} \right] = 2.8 \times 10^{-8} \, T_e \, {\rm [keV]}^{-3/2}$ [21] is used for T_e up to 2.1 keV, above which the resistivity η is set to be uniform. This gives an initial resistivity about $6\eta_{\rm sp}$ on the magnetic axis, $1.4\eta_{\rm sp}$ at q=3/2 and $\eta_{\rm sp}$ for $q \geqslant 2$, which is not expected to affect the simulation results strongly. The parallel heat diffusivity $\kappa_{\parallel} \propto T_e^{5/2}$ follows the Spitzer-Härm formulation [21], while the perpendicular heat diffusivity is set to $2\,{\rm m}^2\,{\rm s}^{-1}$. The perpendicular particle diffusivity is set to $2\,{\rm m}^2\,{\rm s}^{-1}$ and the parallel particle transport is purely convective. The initial central kinematic viscosity acting on the perpendicular flow is set to $4\,{\rm m}^2\,{\rm s}^{-1}$, while the one for the parallel flow is about $40\,{\rm m}^2\,{\rm s}^{-1}$ in the simulations.

A source composed of D_2 neutrals is deposited at the LFS midplane of the plasma, centred at $R = 3.482 \,\mathrm{m}$ and with a Gaussian shape in the toroidal, poloidal and radial directions. The source amplitude and the size of the neutral source (thus that of the plasmoid considering rapid ionization) are varied and will be specified in section 3 together with the simulations.

3. Modelling results and comparison with theory

3.1. Effects of source amplitude

The amplitude of the neutral source is varied in the JOREK simulations to study its effect on plasmoid drift. Specifically, deuterium neutrals are injected at a rate/amplitude ranging from 2×10^{26} to 1×10^{28} deuterium atoms per second and for a duration of $0.05 \,\mu s$, i.e. the total number of injected

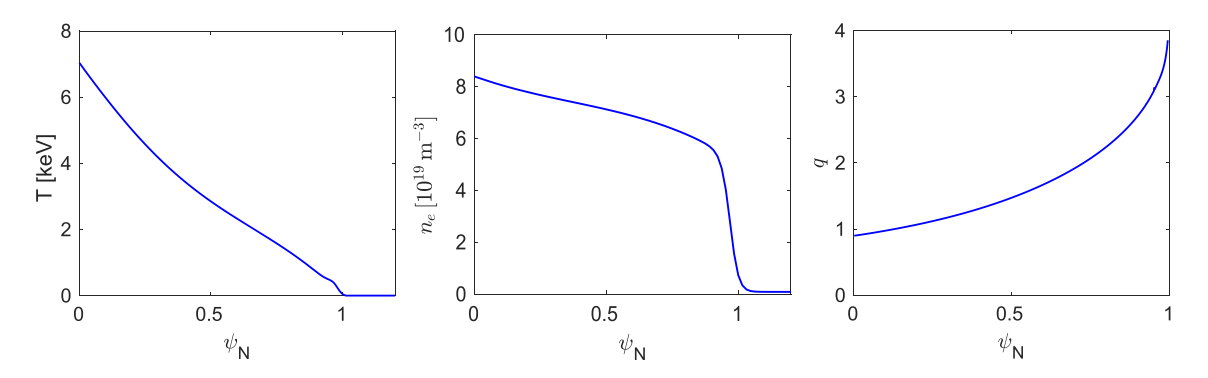


Figure 2. Initial flux-surface-averaged $T = T_i = T_e$, n_e and q profiles used in JOREK.

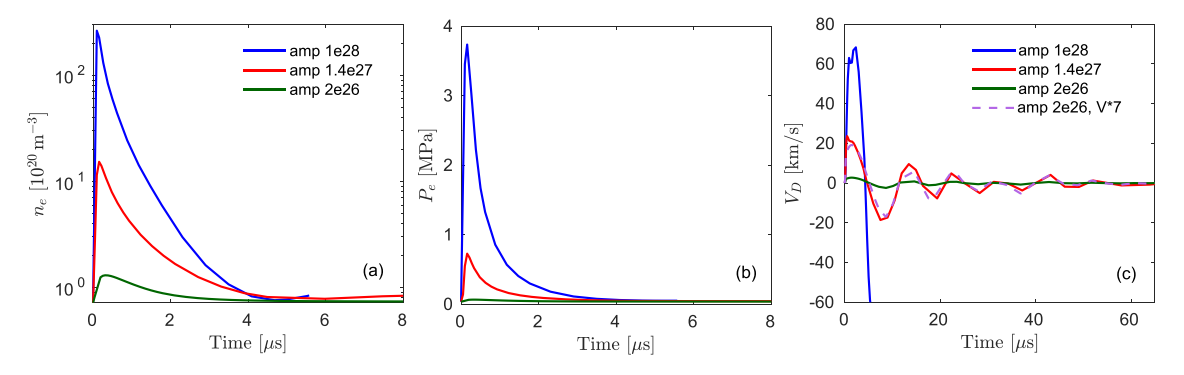


Figure 3. Left to right: Time-evolution of n_e , p_e and V_D evaluated at the source centre (white cross in figure 4) with different neutral injection rates. The number of deuterium atoms injected per second is marked in the legend. The neutral source starts at t = 0 and is cut off at $0.05 \,\mu$ s. Note that (c) shows a wider time window than (a) and (b).

deuterium atoms ranges from 1×10^{19} to 5×10^{20} in the simulations. This corresponds to a pellet with radius of 0.35 to 1.3 mm when assuming a spherical shape, comparable with pellet fueling experiments on JET (with a radius of about $1 \sim 3$ mm [22]). The neutral injection rate, however, is larger than the typical pellet ablation rate on JET, which is on the order of 1×10^{25} s⁻¹ for a pellet with a radius of 2 mm in ohmic discharges with a central T_e about 2 keV[23]. This is due to a much shorter duration of the source deposition in these simulations, which is set to $0.05\,\mu$ s, whereas it takes a few tens of microseconds to establish an ablation cloud [8, 24]. The short source duration was chosen to reduce the computational time as we mainly focus on the plasmoid dynamics after source deposition here.

The initial half e^{-1} width of the neutral cloud in the toroidal, poloidal and radial directions is fixed to $\Delta \phi = 0.5 \, \text{rad}$, $L_{\theta} = 4 \, \text{cm}$ and $\Delta r = 4 \, \text{cm}$, respectively, unless otherwise stated. As discussed in section 1, $\Delta \phi$ here is limited by the achievable toroidal resolution in the simulations and should be larger than 0.32 rad with n up to 10. This corresponds to a half toroidal length on the order of 1 m on JET, which is much larger than the initial half-length of a typical pellet cloud (on the order of 10 cm [8, 24]). We will therefore investigate the effects of using such a toroidally (thus poloidally) elongated source on plasmoid dynamics in this paper (section 3.2).

 n_e , p_e and V_D evaluated at the source centre and thus that of the initial plasmoid (white cross in figure 4) are depicted in figure 3, where V_D is taken from the R component of the $\mathbf{E} \times \mathbf{B}$

velocity by definition. Note that figure 3(c) has a wider time window than (a) and (b) to show the oscillations of V_D that will be discussed below. t=0 in this paper denotes the time when the neutral source starts, i.e. it is cut off at $t=0.05\,\mu\text{s}$. Given the large parallel heat conductivity, the plasmoid temperature equilibrates rapidly with the background plasma in the same flux tube and reaches about $3.3\,\text{keV}$ for cases with an injection rate equal to or smaller than $1.4\times10^{27}\,\text{s}^{-1}$, while the $1\times10^{28}\,\text{s}^{-1}$ case exhibits an initial drop of T_e to around $1\,\text{keV}$ due to strong dilution cooling, not shown here for conciseness.

The local n_e and p_e in figure 3 peak at $t = 0.1 - 0.2 \,\mu\text{s}$ due to fast and strong ionization and gradually decay along with plasmoid expansion. V_D initially increases due to the imbalanced pressure (first term on the RHS of equation (1)) and quickly saturates (within a few microseconds) via the braking effects that will be discussed below. The distribution of the $\mathbf{E} \times \mathbf{B}$ flow potential U and thus V_D oscillates (covering negative values) during the deceleration of plasmoid drift as it takes some time for the perturbation caused by the plasmoid drift to decay (related to the resistance of the parallel current channel). As shown in figure 3(c), V_D returns to about 0 at $t \approx 60 \,\mu\text{s}$ for the $1.4 \times 10^{27} \,\text{s}^{-1}$ case (referred to as 'the amp- 1.4×10^{27} case' hereafter and similarly for the other cases) and the amp-2 \times 10²⁶ case, while the simulation of the 1 \times 10²⁸ case only reaches $t \approx 5.5 \,\mu\text{s}$ due to numerical issues. This happens after about 240 simulation time steps since the plasmoid has reached the computational boundary (4.1 μ s in figure 4) and is not expected to affect the main analyses here. In the rest of the

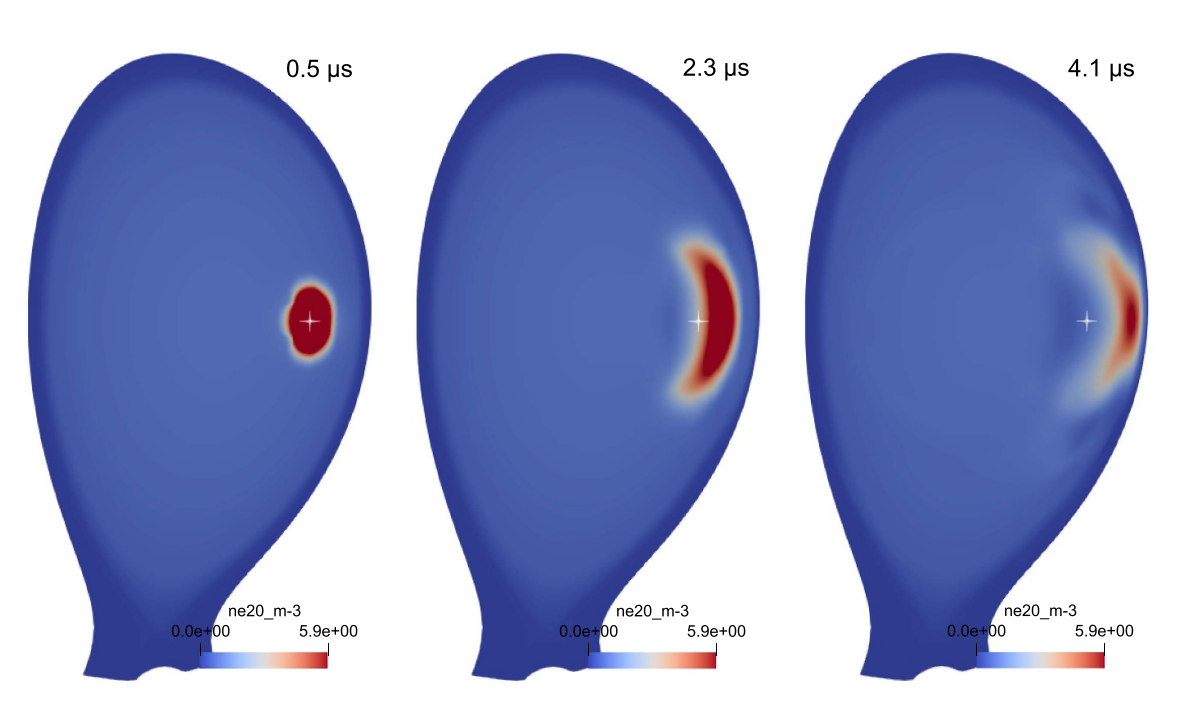


Figure 4. Left to right: n_e at different time of the 1×10^{28} case (blue traces in figure 3) on the neutral source injection plane. The white crosses mark the centre of the neutral source and thus that of the initial plasmoid.

paper we will only focus on the narrow time window to study the early acceleration and saturation of the plasma drift.

One may infer the main braking mechanism at play via the dependence of $V_{\rm D,lim}$ on the source amplitude, which according to equation (2) has a linear dependence on plasmoid pressure (thus source amplitude) when the SAW braking mechanism dominates. As shown by the dashed purple line in figure 3(c), V_D of the amp-2 × 10²⁶ case matches well with that of the amp- 1.4×10^{27} case (red) when scaling it up by a factor of 7. This implies that the SAW braking dominates in these cases with relatively small source amplitude. The existence of the SAWs in the simulations will be detailed in section 4. The case with a much higher source amplitude (the 1×10^{28} case), however, has a $V_{D,lim}$ that is much lower than one would obtain from scaling its V_D based on the source amplitude, i.e. about 65 km s⁻¹ in the figure versus 130 km s⁻¹ expected from the scaling. One possible explanation for this is that the Pégourié braking and thus the total braking effect is stronger with larger source amplitude, despite the SAW braking is weaker (second term on the RHS of equation (1)). The hypothesis of strong Pégourié braking in the case of very large source amplitude could be supported by the strong stochastization of magnetic field lines in this case (figure 12), which would allow more efficient field line mixing and development of 3D parallel res-

The large V_D in the 1×10^{28} case shown in figure 3 leads to an evident outward displacement of the plasmoid along the R direction within the time window of interest, as illustrated in figure 4. The plasmoid largely deviates from its original location at $t\approx2.3\,\mu\rm s$, explaining the drop of V_D (evaluated at the source centre) at $t\approx2.3\,\mu\rm s$ in figure 3(blue case). The plasmoid starts to reach the computational boundary at about $4.1\,\mu\rm s$. The average drift velocity of the plasmoid at

 $t=[2.3\,4.1]\,\mu s$, estimated based on the drift distance seen in figure 4 and the corresponding time interval, is still about $65\,{\rm km\,s^{-1}}$, confirming the level of $V_{\rm D,lim}$ in this case. Note that V_D already saturates to about $65\,{\rm km\,s^{-1}}$ at about $1\,\mu s$, i.e. well before the evident outward displacement of the plasmoid. Regarding the cases with smaller source amplitude, the amp- 1.4×10^{27} case does not show a large deviation of the plasmoid from its original location until $t\approx3.5\,\mu s$, i.e. some time after reaching its $V_{\rm D,lim}$, while the amp- 2×10^{26} case does not exhibit evident displacement in the time window of interest due to its small V_D . This confirms that the saturated velocity shown in figure 3 represents the actual $V_{\rm D,lim}$ of the plasmoid in these cases.

3.2. Effects of source toroidal extent

We have seen from the previous section that the SAW braking contributes strongly to $V_{\rm D,lim}$ in cases with a relatively small source amplitude, i.e. with an injection rate up to $1.4\times10^{27}\,{\rm s}^{-1}$ in these simulations. In this section, we focus on the amp- 1.4×10^{27} case and investigate the effect of the source toroidal extent on plasmoid drift by varying $\Delta\phi$ from 0.5 to 2 rad in the simulations, as summarized in figure 5. $\Delta r = L_\theta = 4\,{\rm cm}$ is fixed as in the previous section, i.e. the red case is the same as the red case in figure 3. Note that n_e and p_e in figure 5 are not proportional to $\Delta\phi^{-1}$ since the poloidal size of the plasmoid also depends on its toroidal size and thus on $\Delta\phi$, as will be specified in section 3.4.

One noticeable feature of these simulations is the earlier fast drop of V_D with larger $\Delta \phi$, as illustrated by the dashed purple curve in figure 5(c), which is a scaling of the purple case by a factor of 5.7 to match the maxima of the red case

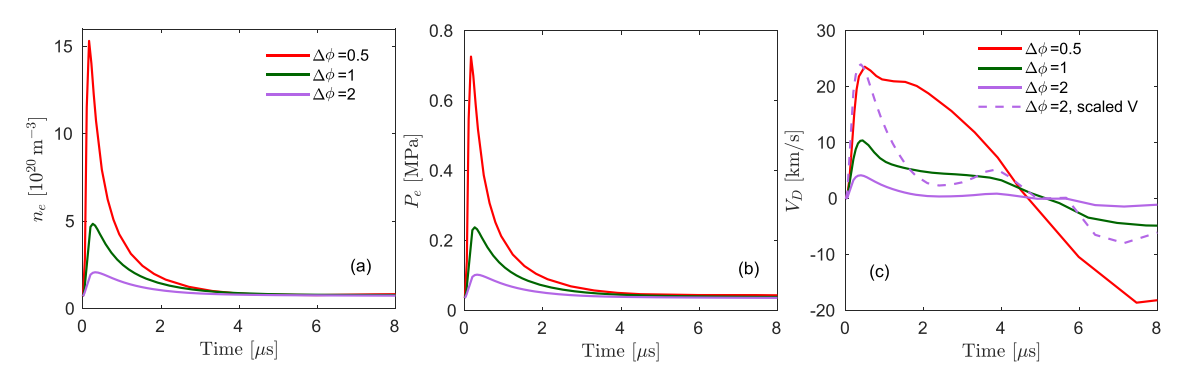


Figure 5. Left to right: Time-evolution of n_e , p_e and V_D evaluated at the source centre with different toroidal extent of the source $\Delta \phi$. The red case is the same as the red case in figure 3. The dashed purple curve is a scaling of the solid purple case (by a factor of 5.7) to help guide the eyes.

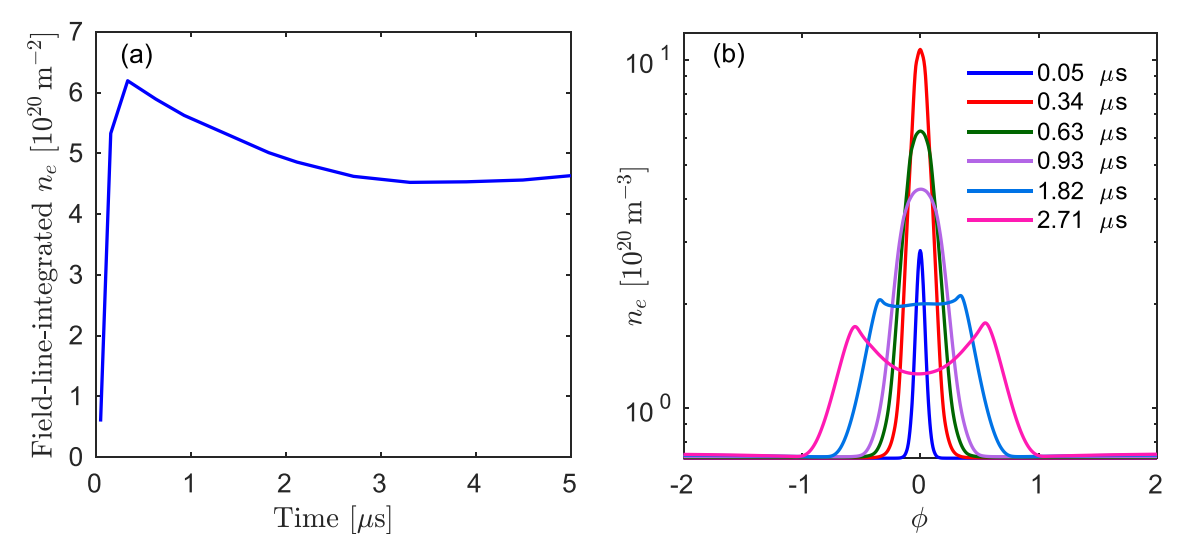


Figure 6. (a) Field-line-integrated plasmoid density of the amp-1.4 × 10^{27} case discussed in section 3.1 and (b) corresponding $n_e(\phi)$ at different time slices marked by the legend. The evaluation is done along the magnetic field line passing through the source centre.

and help guiding the eyes. This can be explained by the earlier onset of the Pégourié braking with larger $\Delta\phi$, i.e. a shorter external plasmoid–plasmoid connection length, as expected from theory [6]. This has important implications for 3D MHD simulations, where the toroidal source extent is typically artificially enlarged due to numerical issues and limitations in computational resources, making it difficult to reach drift levels inferred from experiments [10]. In the rest of the paper we will focus on the cases with relatively small source amplitude and $\Delta\phi=0.5\,\mathrm{rad}$ to concentrate on the effects of the SAW braking on plasmoid drift and aim at a quantitative comparison with the existing theory.

3.3. Comparison with plasmoid drift theory

We have seen from the previous sections that the SAW braking dominates the early evolution of V_D in cases with $\Delta \phi = 0.5$ rad and relatively small source amplitude, i.e. the amp- 2×10^{26} and amp- 1.4×10^{27} cases in these simulations. In this section, we compare the saturated drift velocity obtained from JOREK simulations with the one estimated by theory assuming a circular cross-section plasmoid (equation (2)). Utilizing

 $p_0 \equiv 2eT_e n_e$ in the plasmoid, equation (2) can be formulated as

$$V_{\rm D,lim} \approx \frac{2\mu_0 C_A e T_e n_e Z_0}{RB_\phi^2},\tag{3}$$

where T_e is the plasmoid temperature in eV and e the electron charge. T_e remains almost constant during the expansion and drift of the plasmoid, whereas Z_0 and n_e are time-varying. However, as illustrated in figure 6(a), $2n_eZ_0$, or effectively the field-line-integrated plasmoid density along the magnetic field line passing through the source centre (up to $-\pi$ and π away), varies insubstantially after the local ionization of the neutral source at $t \approx 0.35 \,\mu\text{s}$. This allows the estimation of n_eZ_0 and thus $V_{\text{D,lim}}$ using equation (3). Corresponding $n_e(\phi)$ profiles at different time slices and along the magnetic field line passing through the source centre are depicted in figure 6(b), where $\phi = 0$ refers to the neutral source injection plane.

The example shown in figure 6 is the amp- 1.4×10^{27} case discussed in section 3.1. We take $2n_eZ_0 \approx 5 \times 10^{20} \,\mathrm{m}^{-2}$, which gives rise to a field-line-integrated plasmoid electron pressure about $2.6 \times 10^5 \,\mathrm{Pa} \cdot \mathrm{m}$ considering $T_e \approx 3.3 \,\mathrm{keV}$. This results in $V_{\mathrm{D,lim}} \approx 75 \,\mathrm{km \, s}^{-1}$ based on equation (3), which is

Source amplitude (s ⁻¹)	Equation (3) (circular cross section plasmoid) (km s ⁻¹)	JOREK (elliptic cross section plasmoid) (km s ⁻¹)
1.4×10^{27}	75	20
$ \begin{array}{l} 1 \times 10^{27} \\ 2 \times 10^{26} \end{array} $	42.5 8.4	15 2.7

Table 1. Comparing $V_{D,lim}$ based on formula and simulations.

much higher than that obtained from the JOREK simulation, i.e. about $20 \,\mathrm{km \, s^{-1}}$ as shown by the red curve in figures 3(c)and 5(c). Similarly, $V_{D,lim}$ of cases with smaller source amplitude (i.e. where the SAW braking dominates) have been evaluated, as summarized in table 1. Note that the amp-1 \times 10²⁷ case was not shown in section 3.1 for conciseness. It can be seen that $V_{\rm D,lim}$ evaluated by equation (3) is about 3 – 4 times that obtained from JOREK simulations. A possible explanation for this discrepancy is that equation (3) only considers the magnetic field lines passing through the plasmoid region, whereas in reality more magnetic field lines are 'dragged' and bent by the plasmoid (for reasons that will be discussed in section 3.4), giving rise to stronger SAW braking. This is reflected by the size of the $\mathbf{E} \times \mathbf{B}$ flow region on the poloidal plane and a possibly more appropriate way of applying equation (2) in 3D MHD simulations is using an averaged p_e over the $\mathbf{E} \times \mathbf{B}$ flow region, as will be detailed in the next section.

3.4. Effects of the size of the $\mathbf{E} \times \mathbf{B}$ flow region

Considering the 3D geometry of magnetic field lines, the poloidal size of the $\mathbf{E} \times \mathbf{B}$ flow region is expected to depend on the poloidal size and thus the toroidal size of the plasmoid when $\Delta r/(R\cdot\Delta\phi) < B_\theta/B_\phi$, where B_θ is the poloidal magnetic field. This is well satisfied in these simulations considering $\Delta\phi=0.5\,\mathrm{rad}$, $\Delta r=4\,\mathrm{cm}$, $R=3.482\,\mathrm{m}$ and $B_\theta/B_\phi\approx0.23$ at the location of the plasmoid. As an illustration, the $\mathbf{E}\times\mathbf{B}$ flow region of two cases with the same $\Delta\phi=0.5\,\mathrm{rad}$ of the neutral source but with $\Delta r=L_\theta=4\,\mathrm{cm}$ and 8 cm, respectively, are shown in figure 7. It can be seen that the poloidal size of the $\mathbf{E}\times\mathbf{B}$ flow region are indeed very similar in these two cases.

Time-evolution of n_e , p_e and V_D evaluated at the source centre of these two cases are depicted in figure 8. We note that V_D is also very similar in these two cases despite the very different local n_e and p_e caused by the different size of the plasmoid. This is interpreted as due to the fact that the $\mathbf{E} \times \mathbf{B}$ flow region (very similar in these two cases) covers more magnetic field lines than those within the plasmoid region and plays a more important role in plasmoid drift. The larger size of the $\mathbf{E} \times \mathbf{B}$ flow region with respect to the plasmoid is related to the fact that the flow region has a roughly circular cross section on the poloidal plane since \mathbf{E} is essentially a dipole field, whereas the plasmoid is more poloidally elongated than radially, as shown in figure 7 and illustrated in figure 9.

More specifically, figure 9 corresponds to the situation where the SAW braking dominates, i.e. similar to figure 1(b)but with a toroidally elongated plasmoid as is typically used in 3D MHD simulations. Figure 9(a) is the view from the tokamak LFS as in figure 1, while figure 9(b) is the view along the magnetic field line and at the location of the SAW front (indicated by the dotted black line in (a)). \mathbf{j}_{pol} in figure 9(b)(green arrows) exhibits a near circular cross section, following the electrostatic potential distribution of a dipole caused by the charge separation. It follows that the radius of the $\mathbf{E} \times \mathbf{B}$ flow region is determined by the distance between the two poles of the dipole, which itself is determined by the toroidal size rather than the radial size of the source, as discussed before. Note also that j_A changes its sign inside the plasmoid, fulfilling the zero-divergence requirement of the plasma current. This is consistent with what is observed in JOREK simulations, for example, the bottom left plot in figure 15 (looking at the poloidal plane passing through the source centre) shows positive current inside the plasmoid and negative outside.

A larger $\mathbf{E} \times \mathbf{B}$ flow region discussed above means that the plasmoid (which carries magnetic field lines with it) has to bend more field lines while drifting and thus experiencing stronger drag from the magnetic tension. To consider this effect, an effective p_0 taking into account the size of the flow region could be a more appropriate parameter to be used when applying equation (2) in 3D MHD simulations. As a crude estimation, we track about 1600 magnetic field lines originating from the flow region marked by the dashed rectangle in figure 7, i.e. for the amp-1.4 \times 10²⁷ case at $t = 1.82 \,\mu s$. The field-line-integrated plasmoid electron pressure, averaged over the number of field lines, is about $7.25 \times 10^4 \,\mathrm{Pa} \cdot \mathrm{m}$, i.e. only about 1/3.6 of that passing through the source centre $(2.6 \times 10^5 \,\mathrm{Pa \cdot m})$. This explains well the discrepancy shown in table 1, where the calculation was performed considering only the pressure at the plasmoid centre.

To further investigate the effects of the $\mathbf{E} \times \mathbf{B}$ flow region, we vary $F_0 \equiv RB_\phi$ (thus B_ϕ) from $0.5F_0$ to $3F_0$ in JOREK simulations, where $F_0 = 8.274\,\mathrm{T}\cdot\mathrm{m}$ is the reference value as used in the previous sections. $\Delta\phi = 0.5\,\mathrm{rad}, \ \Delta r = L_\theta = 4\,\mathrm{cm}$ and an injection rate of 1.4×10^{27} deuterium atoms per second are kept in these scans. As illustrated in figure 10(a), varying F_0 changes the helicity of the magnetic field lines (thus q), which would in turn affect the poloidal size of the plasmoid and the $\mathbf{E} \times \mathbf{B}$ flow region. As shown in

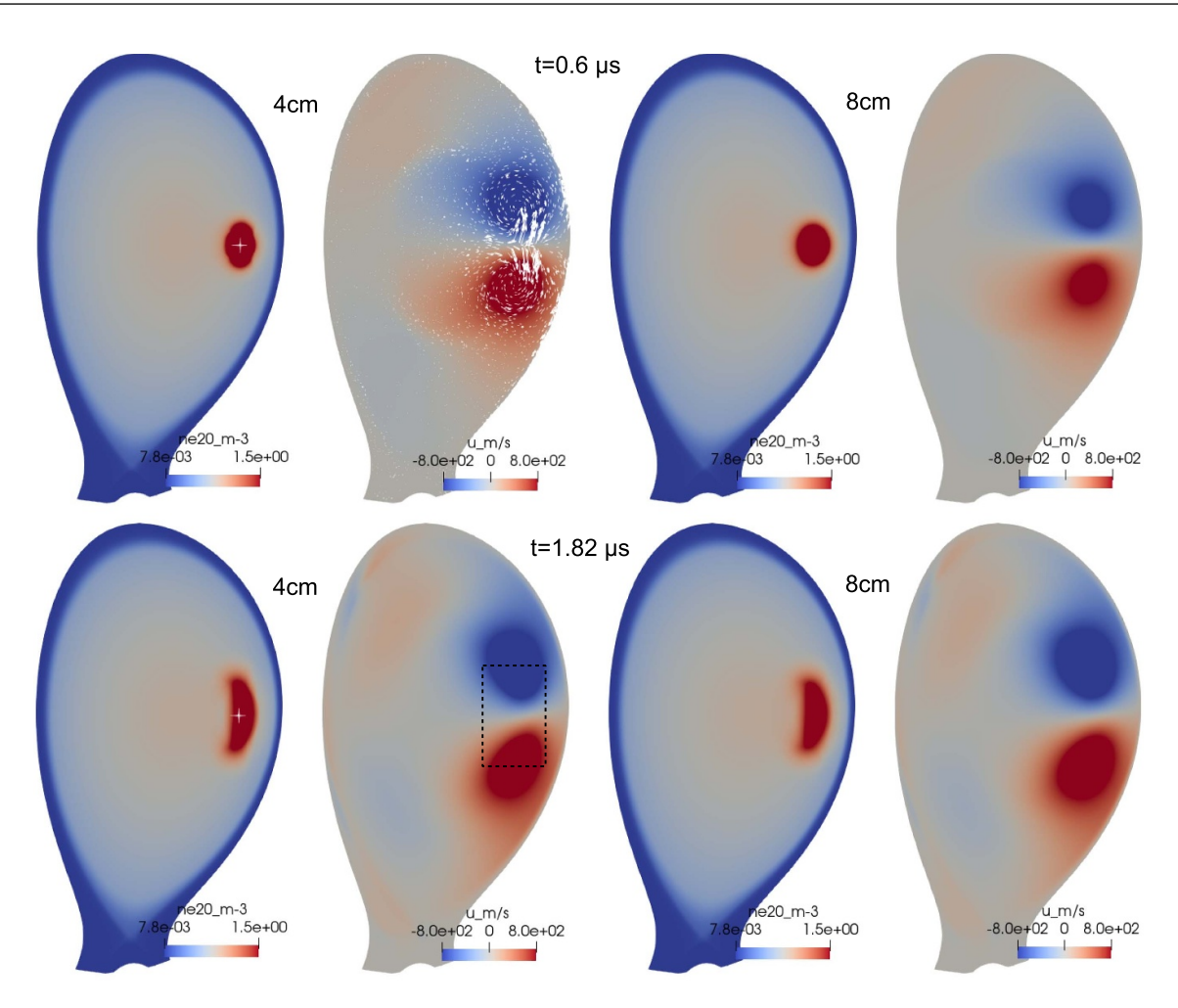


Figure 7. n_e and $\mathbf{E} \times \mathbf{B}$ flow potential U on the neutral source injection plane at $0.6\,\mu s$ (top row) and $1.82\,\mu s$ (bottom) of the two cases shown in figure 8, respectively. The left two columns are with a neutral source with $\Delta r = L_\theta = 4\,\mathrm{cm}$, while the right two are with 8 cm. The white crosses mark the source centre and the white arrows represent the velocity vectors on the poloidal plane. The dashed region illustrates the flow region used for a crude estimation of an effective pressure.

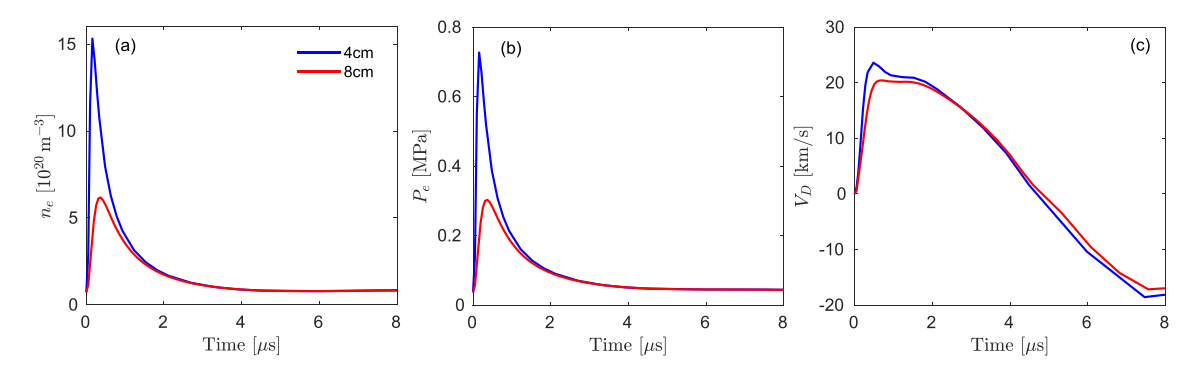


Figure 8. Left to right: Time-evolution of n_e , p_e and V_D with $\Delta r = 4$ cm and 8 cm, respectively. The red case remains the same as the red case in figures 3 and 5.

figure 11, the poloidal size of the plasmoid and the $\mathbf{E} \times \mathbf{B}$ flow region is much smaller with $3F_0$ than with $0.5F_0$, as expected.

As for V_D , two competing effects exist when increasing F_0 (thus B_{ϕ}): the magnetic tension (the B_{ϕ}^2 factor in equation (1)) thus the SAW braking is stronger, which tends to lower V_D ;

the effective volume-averaged p_e is higher due to the smaller size of the $\mathbf{E} \times \mathbf{B}$ flow region, which tends to increase V_D . As shown in figure 10(c), V_D increases with increasing F_0 , indicating that the latter effect is stronger. This once again emphasizes the importance of the size of the $\mathbf{E} \times \mathbf{B}$ flow region on plasmoid drift.

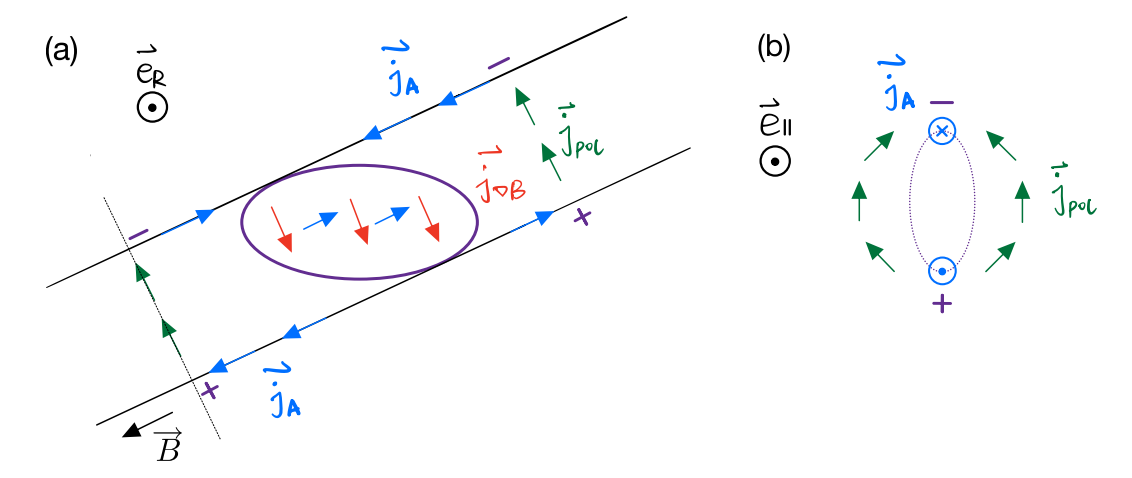


Figure 9. Sketch of plasmoid drift mechanisms of a toroidally elongated plasmoid when $\dot{V}_D = 0$ is reached via the SAW braking. (a) View from the tokamak LFS along the R direction and (b) along the magnetic field line and at the location of the SAW front (dotted black line in (a)). The symbols are elaborated in the text.

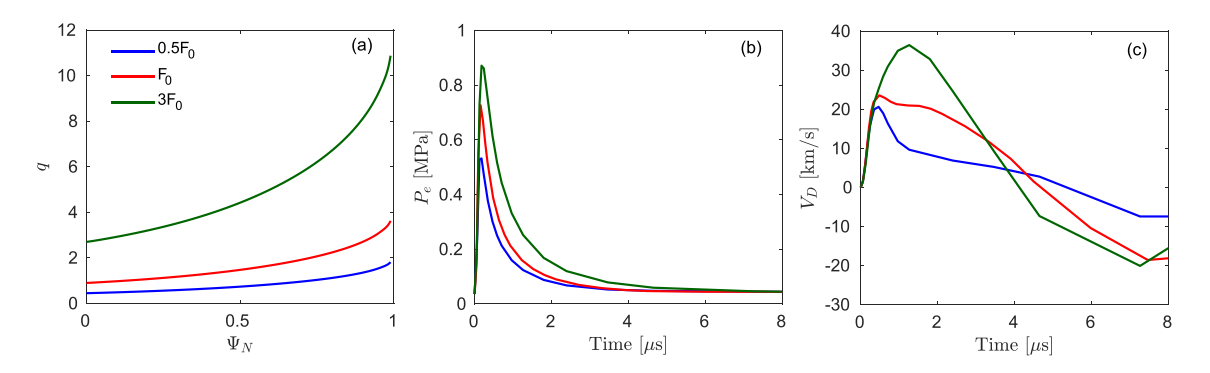


Figure 10. (a) $q(\Psi_N)$ profiles, (b) time-evolution of p_e and (c) V_D in the scans of F_0 .

4. Existence of shear Alfvén waves

4.1. Qualitative observations of shear Alfvén waves

The existence of SAWs can be intuitively inferred from the bending of the magnetic field lines 'dragged' by the drifting plasmoid, as illustrated in figure 12. Here the $R-\phi$ Poincaré map at $t\approx 2.3\,\mu s$ of the 1×10^{28} case discussed in section 3.1 is shown and the location of the source centre is marked by the red cross, exhibiting strong bending of the magnetic field lines. Note that the outer region becomes stochastic in this case due to the strong plasmoid source and thus perturbation imposed. Cases with smaller source amplitude (e.g. amp- 1.4×10^{27} and amp- 2×10^{26}), on the other hand, exhibit weaker bending of the magnetic field lines and the nested flux surfaces remain, though not shown here for conciseness.

Another method to qualitatively observe SAWs is examining the propagation of U along the magnetic field lines, given the fact that SAWs help spread the charges along the field lines at a speed of C_A (i.e. the SAW braking illustrated in figure 1(b)). As an example, U at different time slices of the amp- 2×10^{26} case discussed in section 3.1 is tracked along the magnetic field line passing through the source centre and the resulting U vs. ϕ is shown figure 13. This allows estimating the speed of the parallel propagation of U. At $t\approx1.8\,\mu\text{s}$,

for example, the peaks of U reach $\phi=\pm 2.4\,\mathrm{rad}$, corresponding to a speed of about $4.7\times 10^6\,\mathrm{m\,s^{-1}}$ when considering $B_\phi/B_\theta\approx 4.34$ and $R=3.482\,\mathrm{m}$. This is in good match with $C_A\approx 4.5\times 10^6\,\mathrm{m\,s^{-1}}$ and is consistent with the propagation of SAWs in the simulations.

4.2. Quantification of the shear Alfvén wave energy

To better quantify SAWs, we evaluate the SAW energy, i.e. the volume integral of the square of the perturbed perpendicular magnetic field $(\int \|B_{1,\perp}\|^2 dV)$ based on linear MHD theory [25, 26]. The linear assumption is well held for cases with relatively small source amplitude in these simulations. For example, the perturbed poloidal magnetic flux ψ_1 of the amp-2 × 10²⁶ case discussed in section 3.1 (green case in figure 3) is only on the order of 10^{-3} of the equilibrium value ψ_0 , which barely varies along with time.

Based on the above formulation, time evolution of the volume-integrated SAW energy of the amp- 2×10^{26} case is shown in figure 14(a). It can be seen that the SAW energy increases and reaches a peak at $t \approx 5.5 \,\mu s$. This is in accordance with the evolution of the total perturbed magnetic energy (i.e. sum of all the n > 0 components) shown

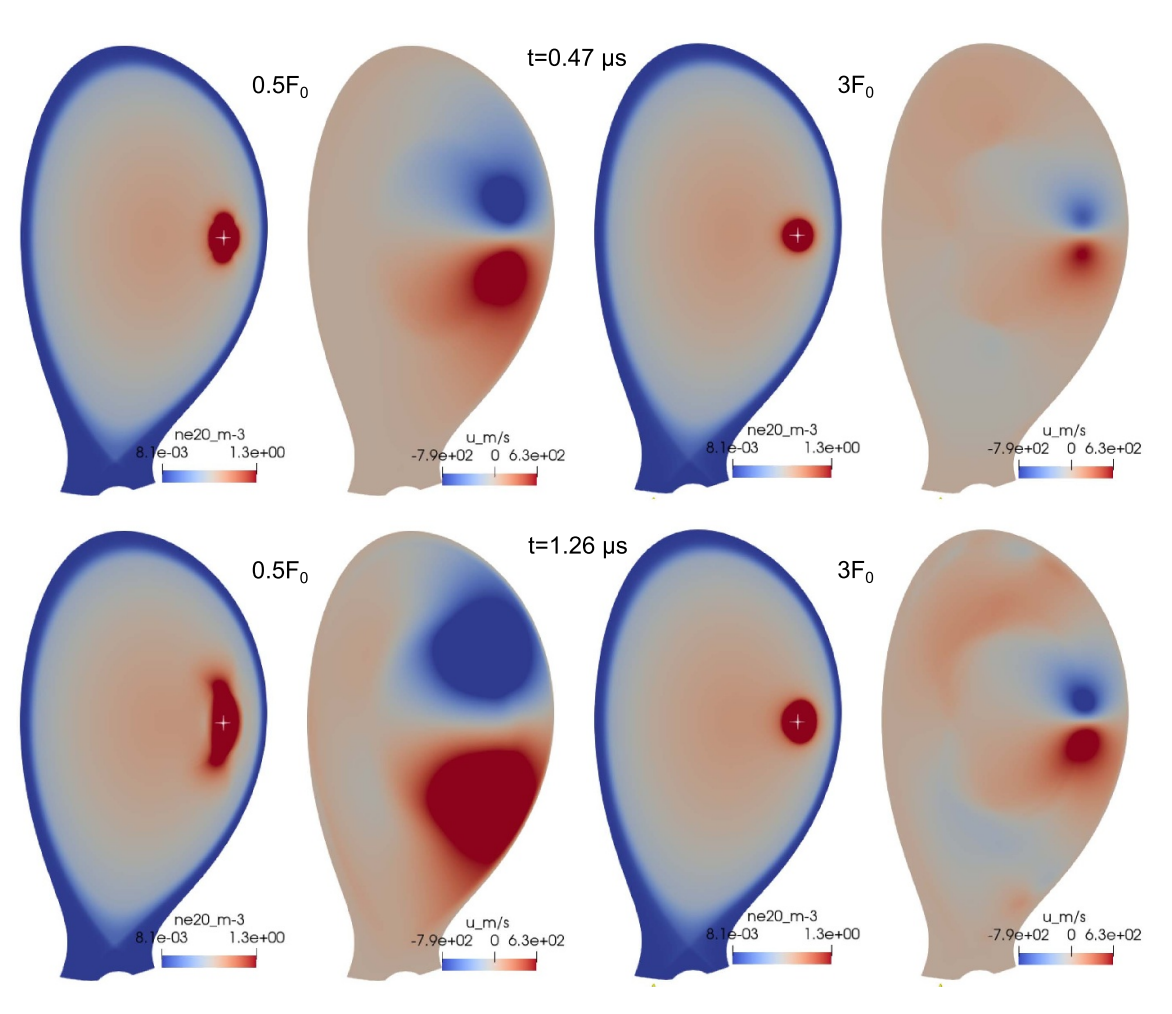


Figure 11. n_e and U on the neutral source injection plane at $0.47 \,\mu s$ (top row) and $1.26 \,\mu s$ (bottom) of two of the cases shown in figure 10, respectively. The left two columns are with $0.5F_0$, while the right two are with $3F_0$. The white crosses mark the source centre.

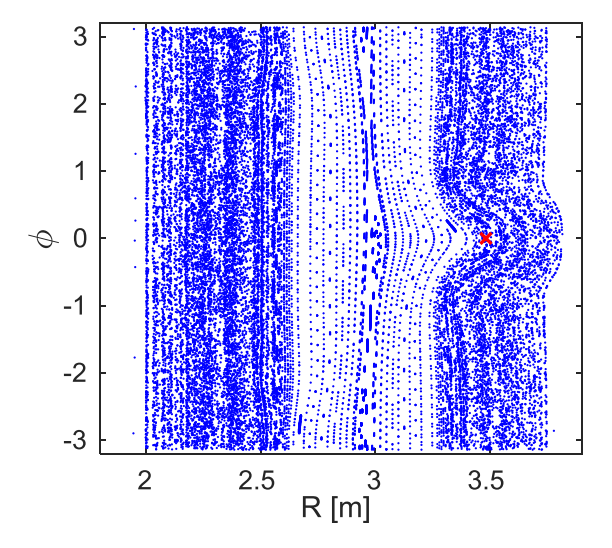


Figure 12. Poincaré map showing the magnetic field line topology on the $R-\phi$ plane and at $t \approx 2.3 \,\mu\text{s}$ of the 1×10^{28} case discussed in section 3.1. The red cross marks the location of the source centre.

in figure 14(b), as expected from the definition of the SAW energy. Corresponding SAW energy density and non-axisymmetric toroidal current density on different poloidal planes are depicted in figures 15 and 16, at $t \approx 3 \,\mu s$ and $5 \,\mu s$,

respectively. We can see that the SAW packets propagate in both directions from the source (at $\phi = 0$) and have finished a toroidal turn at $t \approx 5 \,\mu \text{s}$, allowing a 'mixing' of SAWs from different directions.

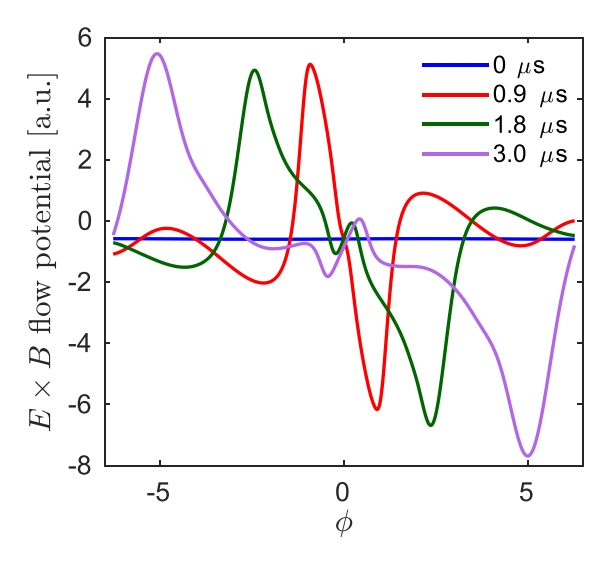


Figure 13. Propagation of the $\mathbf{E} \times \mathbf{B}$ flow potential along the magnetic field line passing through the source centre at different time slices (marked in the legend) of the amp-1.4 \times 10²⁶ case discussed in section 3.1.

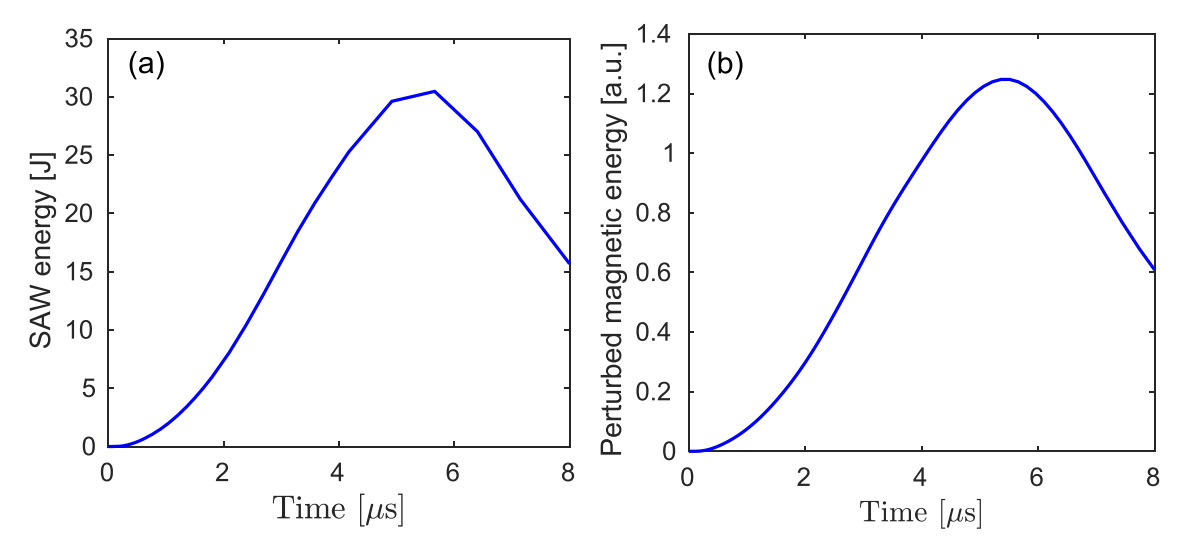


Figure 14. Time evolution of (a) the SAW energy and (b) the total perturbed magnetic energy of the amp- 2×10^{26} case discussed in section 3.1.

5. Conclusions and outlook

Mechanisms of plasmoid drift following MMI have been studied via 3D non-linear MHD modelling with the JOREK code, in particular using a transient pure D_2 neutral source on the LFS midplane of a JET H-mode plasma to facilitate a detailed comparison with existing plasmiod drift theories. The simulations confirm the important role of the propagation of SAWs and the development of external resistive currents along the magnetic field lines in limiting charge separation and thus the $\mathbf{E} \times \mathbf{B}$ plasmoid drift, i.e. the SAW braking and Pégourié braking mechanisms, respectively.

Varying the amplitude of the neutral source, it is found that the drift velocity is limited by the SAW braking on the few microseconds timescale for cases with relatively small source amplitude, as expected from theory. Cases with larger source amplitude, on the other hand, seem to exhibit stronger

Pégourié braking. This is possibly related to stronger stochastization of the magnetic field lines in these cases, allowing more efficient field line mixing and development of 3D parallel resistive currents.

Effects of using a toroidally elongated plasmoid, as is typically adopted in 3D MHD simulations due to limitations in computational resources, are investigated in detail. It was motivated by previous observation that the level of plasmoid drift tends to be underestimated in interpretative 3D modelling of a JET D₂ SPI discharge [10]. With the simplified setup in this paper, it is found that the Pégourié braking sets in earlier with larger toroidal source extent due to shorter external plasmoid-plasmoid connection length, in good agreement with existing theory. The toroidally elongated source also gives rise to stronger Pégourié braking due to smaller resistance of the parallel current channel.

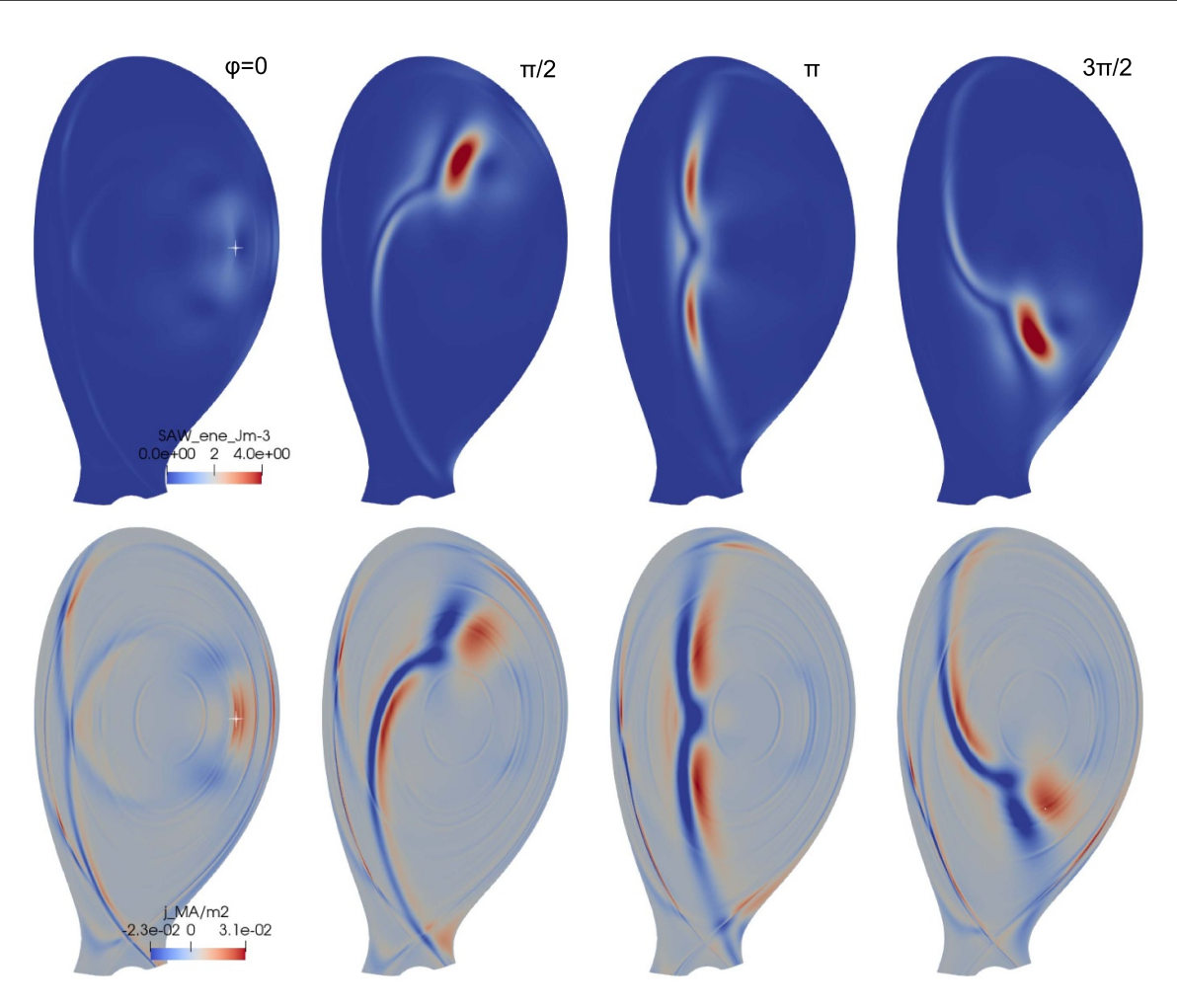


Figure 15. SAW energy density (top) and non-axisymmetric toroidal current density (bottom) at different toroidal locations of the amp-2 \times 10²⁶ case discussed in section 3.1 and at $t \approx 3 \,\mu s$. $\phi = 0$ refers to the neutral source injection plane. The white crosses mark the source centre.

The simplified setup also allows a quantitative comparison with existing plasmoid drift theory, clarifying the effect of the toroidal size of the source on SAW braking. It is found that considering only the plasmoid region in the theoretical formula leads to a higher drift velocity than that from JOREK simulations in the case of a toroidally elongated plasmoid, as summarized in table 1. This is because the toroidally thus poloidally elongated plasmoid results in an elliptic plasmoid cross section on the poloidal plane, whereas the cross section of the $\mathbf{E} \times \mathbf{B}$ flow region remains near circular (as **E** is essentially a dipole field) and covers a larger area than the elliptic plasmoid itself (figure 9(b)). A more realistic and localized pellet cloud, as considered in the plasmoid drift theory, on the other hand, has a circular plasmoid cross section that matches better with its $\mathbf{E} \times \mathbf{B}$ flow region. This means that more magnetic field lines are bent than those contained in the plasmoid region in the case of the elliptic plasmoid, leading to stronger SAW braking and smaller drift velocity. Using a more realistic pellet cloud with a circular cross section in JOREK simulations would match better with the theoretical formula, but is unfortunately not accessible due to the limitation in toroidal resolution mentioned before. Nevertheless, the comparison with theory identifies the key role of the size of the $\mathbf{E} \times \mathbf{B}$ flow region on plasmoid drift and shows that an effective pressure (e.g. a volume-averaged pressure) within the $\mathbf{E} \times \mathbf{B}$ flow region is more applicable in the theoretical formula when considering a toroidally elongated plasmoid as used in 3D MHD modelling. Coupling dedicated codes on pellet physics such as those in [8] and [24] with 3D MHD codes such as JOREK provides a possible solution to model realistic-size plasmoids in 3D MHD simulations.

The existence of SAWs in the simulations is demonstrated, both qualitatively via the field line bending seen in the Poincaré map and the propagation of the $\mathbf{E} \times \mathbf{B}$ flow potential (thus charges) at the Alfvén speed, and quantitatively via the time evolution and spatial distribution of the SAW energy. We also illustrate the plasmoid drift mechanisms discussed in this paper, considering both the situation of a more experimentally relevant spherical plasmoid (figure 1) and the situation of a toroidally elongated plasmoid (figure 9).

The effects of including a small percentage of impurities in the neutral source and using multiple sources will be explored in the future, in view of SPI studies. The former is motivated by the observation that a small amount of impurities could strongly reduce the pressure imbalance of the plasmoid and suppress plasmoid drift [8]. Recent SPI experiments on JET

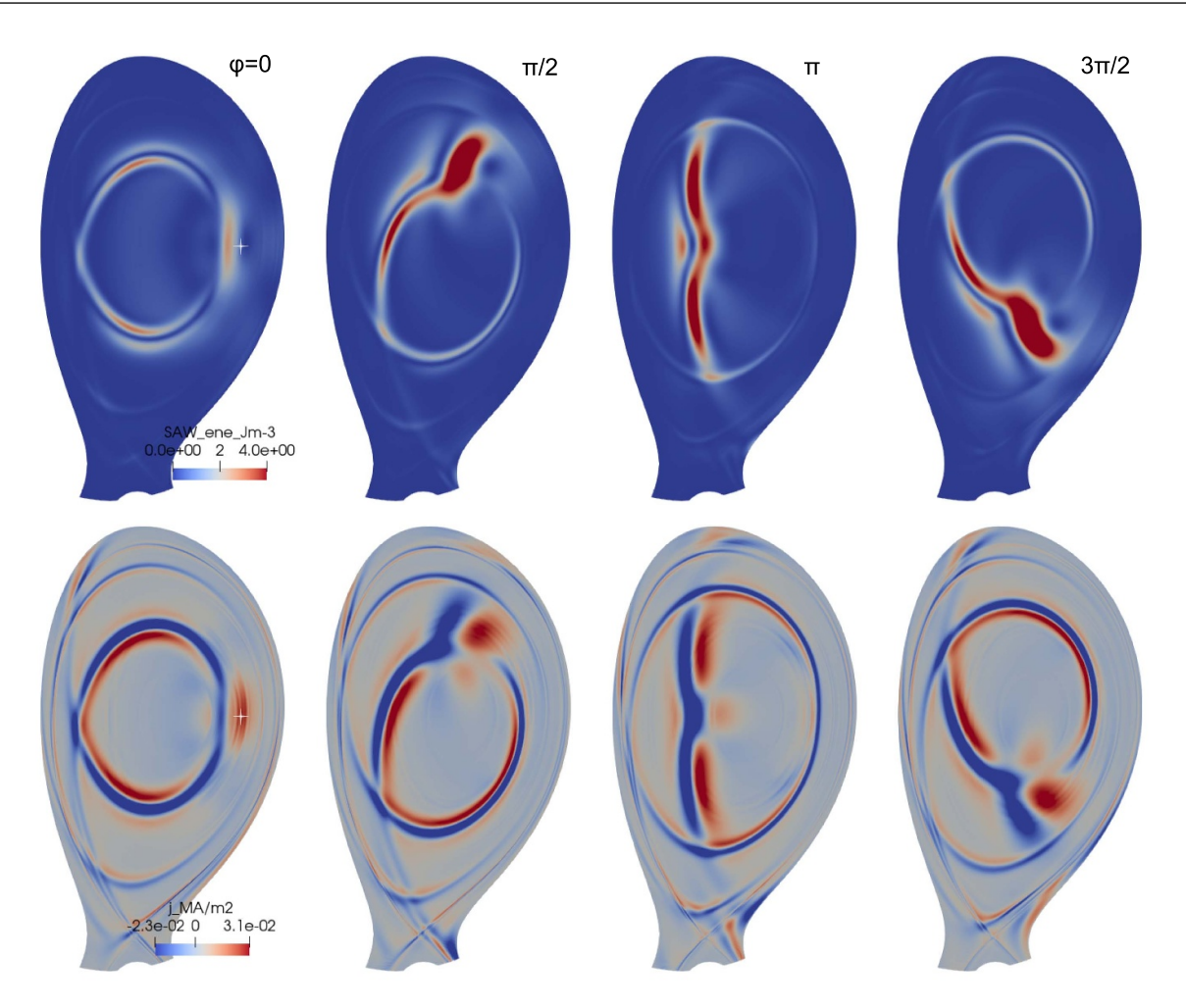


Figure 16. Similar to figure 15, the SAW energy density (top) and non-axisymmetric toroidal current density (bottom) at different toroidal locations of the amp- 2×10^{26} case at $t \approx 5 \,\mu s$.

appear to show similar trend and will be reported elsewhere. The energy transfer from electrons to ions during material assimilation [27] could also affect plasmoid drift and will be considered in future studies.

Acknowledgment

The authors would like to thank B Pégourié, R Ramasamy and F J Artola for fruitful discussions. This work has been carried out within the framework of the EUROfusion Consortium, funded by the European Union via the Euratom Research and Training Programme (Grant Agreement No 101052200 - EUROfusion). The Swiss contribution to this work has been funded by the Swiss State Secretariat for Education, Research ad Innovation (SERI). Views and opinions expressed are however those of the author(s) only and do not necessarily reflect those of the European Union, the European Commission or the SERI. Neither the European Union nor the European Commission nor SERI can be held responsible for them. The JOREK modelling presented were performed on the Marconi-Fusion supercomputer hosted at CINECA. This work was supported in part by the Swiss National Science Foundation.

ORCID iDs

M. Kong https://orcid.org/0000-0002-2004-3513

E. Nardon (1) https://orcid.org/0000-0003-0427-2292

D. Bonfiglio https://orcid.org/0000-0003-2638-317X

M. Hoelzl https://orcid.org/0000-0001-7921-9176

D. Hu https://orcid.org/0000-0001-7099-5734

References

- [1] Jachmich S. et al 2022 Nucl. Fusion 62 026012
- [2] Müller H.W. 1999 Phys. Rev. Lett. 83 2199–202
- [3] Rozhansky V., Veselova I. and Voskoboynikov S. 1995 Plasma Phys. Control. Fusion 37 399–414
- [4] Parks P.B., Sessions W.D. and Baylor L.R. 2000 Phys. Plasmas 7 1968–75
- [5] Rozhansky V. et al 2004 Plasma Phys. Control. Fusion 46 575–91
- [6] Pégourié B. 2007 Nucl. Fusion 47 44-56
- [7] Pégourié B. 2007 Plasma Phys. Control. Fusion 49 R87
- [8] Matsuyama A. 2022 Phys. Plasmas 29 042501
- [9] Vallhagen O. et al 2023 J. Plasma Phys. 89 905890306
- [10] Kong M. et al 2024 Nucl. Fusion 64 066004
- [11] Strauss H.R. and Park W. 1998 Phys. Plasmas 5 2676–86
- [12] Aiba N., Tokuda S., Hayashi T. and Wakatani M. 2004 J. Phys. Soc. Japan 73 364–73

- [13] Ishizaki R. and Nakajima N. 2011 Plasma Phys. Control. Fusion 53 054009
- [14] Hu D. et al 2024 Nucl. Fusion 64 086005
- [15] Hoelzl M. et al 2021 Nucl. Fusion 61 065001
- [16] Hoelzl M. et al 2024 Nucl. Fusion 64 112016
- [17] Fil A. et al 2015 Phys. Plasmas 22 062509
- [18] Hu D. et al 2018 Nucl. Fusion 58 126025
- [19] Pamela S.J. et al 2020 Phys. Plasmas 27 102510
- [20] Korving S.Q., Huijsmans G.T., Park J.S. and Loarte A. 2023 Phys. Plasmas 30 042509
- [21] Spitzer L. and Harm R. 1953 Phys. Rev. 89 977-81
- [22] Baylor L.R. et al 1991 Nucl. Fusion 31 1249-59

- [23] Baylor L.R. et al 1992 Nucl. Fusion 32 2177-87
- [24] Samulyak R., Yuan S., Naitlho N. and Parks P.B. 2021 *Nucl. Fusion* **61** 46007
- [25] Freidberg J. 2014 *Ideal MHD* (Ideal MHD Cambridge University Press)
- [26] Puchmayr J., Dunne M. and Strumberger E. 2022 J. Plasma Phys. 88
- [27] Aleynikov P. *et al* 2020 Energy balance during pellet assimilation International Atomic Energy Agency (IAEA) Preprints 1–8 (available at: https://nucleus.iaea.org/sites/fusionportal/Shared%20Documents/FEC%202020/fec2020-preprints/preprint0898.pdf)